

See discussions, stats, and author profiles for this publication at: <https://www.researchgate.net/publication/6386434>

Crystal Structure of a Hyperactive Escherichia coli Glycerol Kinase Mutant Gly230 → Asp Obtained Using Microfluidic Crystallization Devices †, ‡

ARTICLE in BIOCHEMISTRY · JUNE 2007

Impact Factor: 3.02 · DOI: 10.1021/bi700096p · Source: PubMed

CITATIONS

13

READS

37

6 AUTHORS, INCLUDING:



Byron Delabarre

Agios Pharmaceuticals

22 PUBLICATIONS 1,154 CITATIONS

SEE PROFILE



Anu Raghunathan

CSIR - National Chemical Laboratory, Pune

20 PUBLICATIONS 460 CITATIONS

SEE PROFILE

Crystal Structure of a Hyperactive *Escherichia coli* Glycerol Kinase Mutant Gly230 → Asp Obtained Using Microfluidic Crystallization Devices^{†,‡}

Megan J. Anderson,^{§,||} Byron DeLaBarre,[⊥] Anu Raghunathan,[#] Bernhard O. Palsson,[#] Axel T. Brunger,[⊥] and Stephen R. Quake^{*,||}

Department of Biochemistry and Molecular Biophysics, California Institute of Technology, MS 128-95, Pasadena, California 91125, Department of Bioengineering, Stanford University and Howard Hughes Medical Institute, James H. Clark Center E300, 318 Campus Drive, Stanford, California 94305, Howard Hughes Medical Institute and Departments of Molecular and Cellular Physiology, Neurology and Neurological Sciences, Structural Biology and Stanford Synchrotron Radiation Laboratory, Stanford University, James H. Clark Center E300, 318 Campus Drive, Stanford, California 94305, and Department of Bioengineering, University of California, San Diego, 9500 Gilman Drive, La Jolla, California 92093

Received January 17, 2007; Revised Manuscript Received March 13, 2007

ABSTRACT: The crystal structure of an *Escherichia coli* glycerol kinase mutant Gly230 → Asp (GK^{G230D}) was determined to 2.0 Å resolution using a microfluidics based crystallization platform. The crystallization strategy involved a suite of microfluidic devices that characterized the solubility trends of GK^{G230D}, performed nanoliter volume free interface diffusion crystallization experiments, and produced diffraction-quality crystals for in situ data collection. GK^{G230D} displays increased enzymatic activity and decreased allosteric regulation by the glycolytic pathway intermediate fructose 1,6-bisphosphate (FBP) compared to wild-type GK (GK^{WT}). Structural analysis revealed that the decreased allosteric regulation is a result of the altered FBP binding loop conformations in GK^{G230D} that interfere with the wild-type FBP binding site. The altered FBP binding loop conformations in GK^{G230D} are supported through a series of intramolecular loop interactions. The appearance of Asp230 in the FBP binding loops also repositions the wild-type FBP binding residues away from the FBP binding site. Light scattering analysis confirmed GK^{G230D} is a dimer and is resistant to tetramer formation in the presence of FBP, whereas GK^{WT} dimers are converted into putatively inactive tetramers in the presence of FBP. GK^{G230D} also provides the first structural evidence for multiple GK monomer conformations in the presence of glycerol and in the absence of a nucleotide substrate and verifies that glycerol binding is not responsible for locking GK into the closed conformation necessary for GK activity.

In-depth analysis of *Escherichia coli* metabolism over the past decades has revealed complex, tightly regulated metabolic networks that facilitate optimal growth under diverse environmental conditions. A constraints-based in silico model of *E. coli* metabolism was recently developed and used to predict the optimal growth rates of *E. coli* on various substrates (1). The experimental growth rate for each substrate was determined, and *E. coli* grew at the predicted optimal growth rate on all of the substrates with the exception of glycerol. An adaptive evolution study of *E. coli* growth on glycerol revealed that after 700 generations *E. coli* reached the predicted optimal growth rate for glycerol. Sequence analysis of the evolved *E. coli* identified 10 distinct strains,

seven of which contain mutations in the glycerol kinase gene (2, 3).

Glycerol kinase (GK)¹ is the enzyme responsible for the transfer of the γ -phosphoryl group from ATP to glycerol to produce glycerol-3-phosphate and is the rate-limiting step in glycerol metabolism (4, 5). Under physiological conditions, GK exists in a dimer–tetramer equilibrium where the dimer is active and the tetramer is inactive, although a series of kinetic studies suggest an active tetramer may also exist (6–8). GK dimers exhibit “half-of-the-sites binding” for glycerol and ATP substrates, in which one monomer has a high-affinity active site and the other has a low-affinity active site (9). GK is a member of the ATPase superfamily and shares a common $\beta\beta\alpha\beta\alpha\beta\alpha$ tertiary fold and catalytic mechanism with actin, hexokinase, and the heat shock protein 70 (10). GK undergoes a large conformational change from an open to a closed form during enzymatic activity similar to actin and hexokinase, although the conformational change occurs at a different stage in GK activity (11–14).

[†] This work was supported in part by the Howard Hughes Medical Institute and the NIH Director’s Pioneer Award to S.R.Q.

[‡] The Brookhaven Protein Data Bank code for GK^{G230D} is 2P3R.

^{*} To whom correspondence should be addressed. Phone: (650) 736-7890. Fax: (650) 736-1961. E-mail: quake@stanford.edu.

[§] California Institute of Technology.

^{||} Department of Bioengineering, Stanford University and Howard Hughes Medical Institute.

[⊥] Howard Hughes Medical Institute and Departments of Molecular and Cellular Physiology, Neurology and Neurological Sciences, Structural Biology and Stanford Synchrotron Radiation Laboratory, Stanford University.

[#] Department of Bioengineering, University of California.

¹ Abbreviations: GK, glycerol kinase; FBP, fructose 1,6-bisphosphate; PTS, phosphotransferase system; SEC-MALLS, size exclusion chromatography - multi-angle laser light scattering studies; NCS, noncrystallographic symmetry; asu, asymmetric unit; rmsd, root-mean-square deviation; ATF, phosphodifluoromethylphosphonic acid-adenylate ester.

Allosteric regulation of GK activity is necessary to prevent the accumulation of toxic levels of glycolytic intermediates and to promote the preferential use of glucose over glycerol. GK activity is regulated by two distinct allosteric effectors: the sugar phosphotransferase system (PTS) phosphocarrier protein IIA^{Glc} (15, 16) and the glycolytic pathway intermediate fructose 1,6-bisphosphate (FBP) (17). The PTS protein IIA^{Glc} inhibits GK activity in the presence of glucose by binding to a coil and an α -helix on the surface of GK and transforming the region into a 3₁₀ helix (18, 19). One IIA^{Glc} molecule is bound per GK monomer at a position near the dimer interface and opposite the tetramer interface.

Feedback inhibition by FBP involves the formation and stabilization of an inactive tetrameric form of GK. Two FBP molecules are bound per GK tetramer with one-half of the FBP binding site contributed by an FBP binding loop in each monomer at the tetramer interface (20). The sequence of the FBP binding loop is similar to a Walker-type nucleotide phosphate binding loop (residues 229–236 IGGKGGTR (21); Walker-type motif GxxGxGKT/S). Although Walker-type loops in ATP binding proteins are traditionally involved in nucleotide binding, the FBP binding loops bind to the 1- and 6-phosphate moieties of FBP (20). FBP regulation of GK is dependent on tetramer formation and disruption of the GK tetramer interface eliminates FBP inhibition (11, 20, 22, 23).

Notably, six of the seven GK mutations identified during the above-mentioned adaptive evolution experiments occurred at the FBP binding site and the tetramer interface in regions associated with FBP regulation. The mutation that appeared with the greatest frequency was located in the FBP binding loop at Gly230 → Asp (GK^{G230D}). Kinetic investigation of GK^{G230D} revealed a 12-fold increase in enzyme activity and a 33% decrease in FBP inhibition compared to wild-type GK (GK^{WT}) (2). We solved the crystal structure of GK^{G230D} to investigate the increased activity and altered allosteric regulation of this hyperactive glycerol kinase mutant. The crystal structure of GK^{G230D} was obtained using a microfluidic crystallization platform and is the first demonstration of in situ structure determination for a novel crystallization target.

EXPERIMENTAL PROCEDURES

Protein Expression and Purification. *E. coli* GK^{G230D} DNA was obtained from previous adaptive evolution studies (1–3) and cloned into a pETBlue-2 vector (Novagen) to introduce a C-terminal His₆-Tag (2). Protein expression and purification were performed as previously described with minor modifications (24, 25). All purification steps were performed in standard buffer (20 mM Tris·HCl (pH 7.5), 10 mM glycerol, 1 mM β -mercaptoethanol) at 4 °C excluding the affinity chromatography purification. Briefly, GK^{G230D} was transformed into *E. coli* BL21(DE3)pLysS cells (Invitrogen) and expression was induced with 1 mM IPTG for 4 h before the cells were harvested by sonication. The protein was purified by metal-chelate affinity chromatography using a Ni-NTA column (25), anion exchange chromatography using a Mono Q 5/50 GL column (GE Life Sciences), and gel filtration chromatography using a Superdex 200 10/30 GL column (GE Life Sciences). The purified protein was concentrated to 30 mg/mL and stored in standard buffer at –80 °C.

The activity of GK^{G230D} was measured using an ADP-coupled assay (9) and compared to the activity of GK^{WT} using commercially available lyophilized *E. coli* GK^{WT} (Fluka). GK^{G230D} and GK^{WT} activity was on the order of the previously published values (2, 9). All enzyme standards and chemicals for the assay were purchased from Sigma-Aldrich.

Size Exclusion Chromatography - Multi-Angle Laser Light Scattering Studies. A DAWN EOS (Wyatt Technology) equipped with a K5 flow cell and a 30 mW linearly polarized GaAs laser of wavelength 690 nm was used in all experiments. The construction, principles, and operation of this apparatus were previously described (26, 27). All measurements were made in the in-line flow mode. Elution buffer (standard buffer \pm 1 mM FBP) was pumped at 0.5 mL/min through a Shimadzu DGU-14A degasser (Shimadzu Corp.) onto a Shodex KW-804 gel filtration column (Shoko America) and 100 μ L of 2 mg/mL protein were injected into the system for each analysis. GK^{G230D} was purified as described above and GK^{WT} was purchased from Fluka. Protein concentration was determined with an Optilab Rex refractive index detector, using a value of 0.185 mL/g for dn/dc. Light scattering data was measured by 12 detectors ranging from 34.8° to 142.5°. The detector responses were normalized by measuring the signal from monomeric bovine serum albumin. The temperature of the light scattering unit and the refractometer were maintained at 25 °C, and the column and all external connections were at ambient temperature.

Solubility Characterization and Crystallization. A microfluidic formulator device was used to characterize the solubility of GK^{G230D} and to generate phase diagrams for crystallization experiments. The solubility screening was performed as previously described with minor modifications in the experimental setup (28, 29). GK^{G230D} was screened with 680 unique reagents produced using 17 salt solutions, 5 buffering agents, and 8 precipitating agents. The salt solutions used were 4 M ammonium acetate, 3 M sodium acetate, 5 M ammonium chloride, 5 M sodium chloride, 4 M ammonium sulfate, 7 M sodium nitrate, 2 M sodium thiosulfate, 2 M lithium sulfate, 6 M sodium formate, 2 M magnesium acetate, 2 M magnesium chloride, 2 M magnesium sulfate, 5 M potassium acetate, 3 M potassium chloride, 2 M potassium phosphate, 4 M sodium phosphate, and 2 M lithium chloride. The buffering agents used were 1 M citric acid (pH 3.5), 1 M MES (pH 6.5), 1 M Hepes (pH 7.5), 1 M Tris·HCl (pH 8.5), and 1 M TAPS (pH 9.5). The precipitants used were the salt solutions (listed above), 100% PEG 300, 100% PEG 550 MME, 50% PEG 1500, 50% PEG 3350, 50% PEG 5000 MME, 50% PEG 8000, and 30% PEG 20000. GK^{G230D} was used at a stock concentration of 30 mg/mL for all solubility and crystallization experiments. Each reagent was screened at six different protein and precipitant concentrations while holding the salt solution and buffering agent at a fixed level (10% of the concentration listed above). The six points screened were (i) 70% precipitating agent, 5% GK^{G230D}, (ii) 60% precipitating agent, 15% GK^{G230D}, (iii) 45% precipitating agent, 30% GK^{G230D}, (iv) 30% precipitating agent, 45% GK^{G230D}, (v) 15% precipitating agent, 60% GK^{G230D}, and (vi) 5% precipitating agent, 70% GK^{G230D}. Protein aggregation was quantified as previously described, and reagents that caused protein aggregation above 2 pixel intensity standard deviation units were classified as crystal-

lization reagents. Phase diagrams were generated for a subset of the identified crystallization reagents as previously described (28, 29). Each phase diagram screened GK^{G230D} solubility at 64 different protein and precipitating agent combinations (between 5 and 75% of the stock concentrations), while the salt solution and buffering agent were held at a constant concentration (10% of the stock concentration listed above). Positions with protein aggregation above 2 pixel intensity standard deviation units were categorized as insoluble and positions with protein aggregation below 2 were categorized as soluble.

Initial crystallization experiments were performed using a modified microfluidic free interface diffusion screening device as described in Anderson et al. (29). Crystals formed after one week at ambient temperature and the best crystallization condition (0.3 M magnesium chloride, 0.1 M Tris·HCl (pH 8.5), and 20% PEG 1500) was transported to microfluidic scale-up diffraction devices. Device fabrication and experimental setup for the scale-up diffraction devices were previously described (30). Crystals appeared in the scale-up diffraction devices after one week at ambient temperature. Sections of the scale-up diffraction device surrounding the crystals were removed from the rest of the device and flash-frozen for in situ diffraction analysis. Cryoprotectant (30% ethylene glycol) was introduced into the diffraction devices by diffusion 1 h before flash-freezing the crystals within the diffraction devices. Vapor diffusion crystallization experiments were performed in parallel and crystals appeared after one week at ambient temperature using the crystallization condition 0.1 M magnesium chloride, 0.1 M Tris·HCl (pH 8.5), and 10% PEG 1500. The crystals were flash-frozen using 30% ethylene glycol as a cryoprotectant.

Data Collection and Processing. Data sets for GK^{G230D} crystals were collected at station 11.3 of the Stanford Linear Accelerator Center (Stanford University) at an incident wavelength of 1.0 Å with a 1° oscillation. Data sets were collected to 2.0 Å resolution from a crystal grown in a scale-up diffraction device and to 3.0 Å resolution from a vapor diffusion crystal for comparison. The data sets were indexed and scaled using DENZO and SCALEPACK and the data set from the scale-up diffraction device was used for structure determination (31).

Structural Determination and Refinement. The phases for the diffraction data were determined by molecular replacement using a monomer from the PDB structure 1GLF as a search model. The “fastdirect” method as implemented in CNS (32) was used to search with one monomer at a time until eight monomers were placed within the asymmetric unit (asu). The asu contained two complete tetrameric species. Noncrystallographic symmetry (NCS) restraints were applied such that corresponding protomers between the two tetramers were restrained. The initial round of minimization and group B factor refinement resulted in a starting R/R_{free} value of 38.7/42.3. Simulated annealing did not improve the structure, so iterative rounds of manual rebuilding with O (33) and minimization/B factor refinement in CNS were used to further the structure refinement. Rebuilding was focused on addressing the hinge motion that created a variety of positions for the second lobe (~residues 250–500) of the different protomers. Eight glycerol molecules were placed into well-defined electron density in each of the active sites. NCS

Table 1: Data Collection and Refinement Statistics for GK^{G230D}

Data collection	
wavelength (Å)	1.0
space group	$P2_1$
cell dimensions	
a (Å)	91.1
b (Å)	114.3
c (Å)	212.6
β (°)	91.1
resolution ^a (Å)	50–2.0 (2.1–2.0)
unique observations ^a	250186 (21731)
redundancy ^a	5.9 (3.4)
completeness ^a	84.0 (73.2) ^f
$I/\sigma(I)$ ^a	36.8 (6.6)
R_{sym} ^b	5.9 (22.5)
Refinement	
resolution (Å)	20–2.0
no. of reflections	221751
no. of refined protein atoms	31752
no. of refined solvent atoms	638
no. of glycerol molecules	8
R_{cryst} ^c	21.0
R_{free} ^d	25.9
average B-factor (Å ²)	21.2
bond length rmsd (Å)	0.018
angle rmsd (°)	1.74
Ramachandran plot	90.7/8.8/0.3/0.2
(% in most favored/allowed/ generous/disallowed regions ^e)	

^a Numbers in parenthesis refer to the highest resolution shell. ^b $R_{\text{sym}} = \sum_j |I_i(j) - \langle I(j) \rangle| / \sum_j I_i(j)$, where $I_i(j)$ is the intensity of the i th observation of reflection j , $\langle I(j) \rangle$ is the weighted mean of all measurements of j . ^c $R_{\text{cryst}} = \sum_j |F_o(j) - F_c(j)| / \sum_j |F_o(j)|$, where F_o and F_c are the observed and calculated structure factors. ^d $R_{\text{free}} = R_{\text{cryst}}$ calculated by using 10% of the reflection data chosen randomly and omitted from the start of refinement (38). ^e The residues in the disallowed regions were found in the active site interacting with glycerol. ^f The limited completeness was due to background scattering produced by the in situ diffraction device in certain directions.

restraints were removed completely at this point. The combined effect of these changes enabled a reduction in the R/R_{free} to 26.6/30.5 through alternating minimization and grouped B factor refinement. The addition of 638 water molecules further reduced the R/R_{free} values to 23.5/27.3. Several regions of the protein did not have clear electron density and were set to 0 occupancy at this point. These regions are segment X_I, residues 229–234 and 501–509; segment O_I, residues 229–235; segment Z_I, residues 498–511; segment X_{II}, residues 229–235 and 324–327; segment Y_{II}, residues 229–235 and 324–327; segment O_{II}, residues 229–234 and residue 463; segment Z_{II}, residues 229–235. The correct orientation of several side chains were established by analyzing likely hydrogen-bonding patterns (34). TLS refinement, as implemented in Refmac (35), was used in the final stages. B factors were reset to 20 before attempting TLS and refined immediately following TLS as restrained individual B factors. The X-ray/geometry weight was optimized to 1.0 to yield the final R/R_{free} values of 21.0/25.9. The data collection and refinement statistics are presented in Table 1.

Domain Motion Analysis. The analysis was performed with the Hingefind algorithm, as implemented in VMD (36). A partition value of 1.8 Å was used for all measurements. The rotation axis defining the two domains in the GK^{G230D} monomers was essentially identical to that found by Bystrom et al. (11). Root-mean-square deviation (rmsd) values were

calculated by superpositioning the C $_{\alpha}$ atoms of residues 2–499 from one monomer onto the second monomer.

RESULTS

Microfluidic Crystallization Strategy for GK^{G230D}. The microfluidics based crystallization platform for GK^{G230D} involved a suite of microfluidic devices that characterized the solubility trends of GK^{G230D} to create a rational crystallization screen, performed hundreds of parallel free interface diffusion crystallization experiments, transported initial crystal hits into larger-scale free interface diffusion experiments, and allowed for in situ data collection from diffraction-quality crystals. The microfluidic crystallization platform enabled nanoliter volume solubility characterization and crystallization experiments and eliminated the necessity of crystal harvesting before data collection.

The crystallization scheme began with a comprehensive characterization of GK^{G230D} solubility using a microfluidic formulator device (28). GK^{G230D} was systematically screened against 680 reagents with distinct salt, buffer, and precipitant components, and reagents that caused protein aggregation were classified as potential crystallization reagents (Figure 1A). Protein phase behavior was broadly screened in response to each reagent by measuring GK^{G230D} solubility at six positions on the phase diagrams. The solubility characterization of GK^{G230D} included a total of 4,080 solubility experiments, and 28% of the reagents were identified as potential crystallization reagents. GK^{G230D} aggregation occurred with the highest frequency for reagents that contained one of the following components: magnesium sulfate salt, sodium phosphate salt, citric acid (pH 3.5) buffer, and PEG 20000 precipitant. Following the broad solubility characterization, complete phase diagrams were generated for GK^{G230D} with a subset of the identified crystallization reagents (Figure 1B). Phase diagrams outline the solubility regimes of a protein in combination with a reagent and are used to design crystallization conditions that target the solubility boundary of a protein. Each complete phase diagram measured GK^{G230D} solubility at 64 different positions and protein aggregation was used to map the insoluble region of the phase diagram. The identified crystallization reagents and the phase behavior information were incorporated into a customized crystallization screen for GK^{G230D}.

The crystallization screen for GK^{G230D} was implemented using microfluidic free interface diffusion screening devices, and 16% of the reagents produced crystals (29, 37). Crystal hits were observed most frequently for crystallization conditions with one of the following components: potassium acetate salt, TAPS (pH 9.5) buffer, and PEG 1500 precipitant. Optimization of the best initial crystallization condition improved crystal size and morphology and produced rhombohedral crystals of dimensions 200 μm \times 150 μm \times 50 μm . The crystallization condition was transported to a microfluidic scale-up diffraction device (30) to produce rhombohedral crystals of dimensions 500 μm \times 200 μm \times 100 μm (Figure 1C). The scale-up diffraction device was designed to produce large crystals encapsulated within a thin layer of elastomeric material to allow for diffraction analysis of the crystals directly through the device. Once crystals appeared in the scale-up diffraction device, a small section of the device surrounding the crystal was cut out and

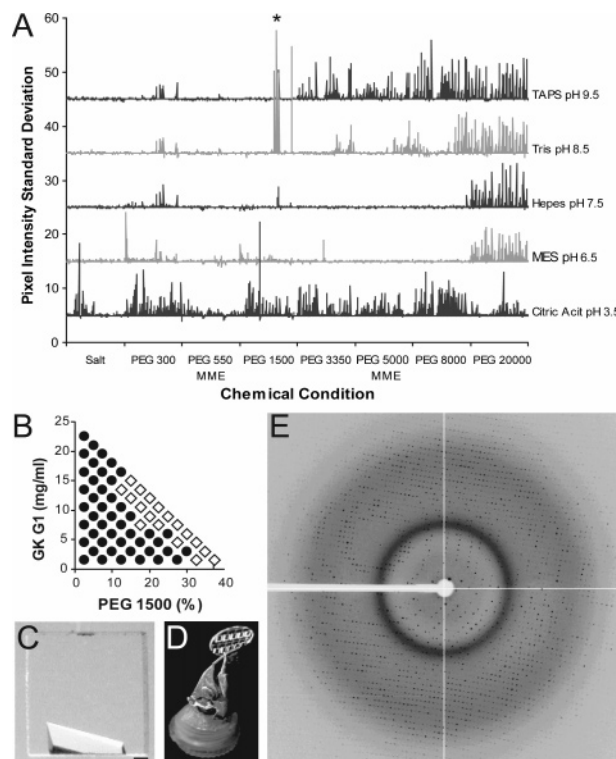


FIGURE 1: Phase behavior characterization and crystallization of GK^{G230D}. (A) Solubility screening results of GK^{G230D} with potential crystallization reagents. The reagents are displayed on separate lines according to buffer composition, and each line is divided by precipitant composition and subdivided by salt composition. The solubility results for the crystallization reagent used for structure determination are highlighted with an asterisk. Pixel intensity standard deviation represents the amount of protein aggregation seen in response to each reagent. A list of the reagents screened is provided in Experimental Procedures. (B) Detailed phase diagram for GK^{G230D} with the crystallization reagent 0.2 M magnesium chloride, 0.1 M Tris-HCl (pH 8.5), and PEG 1500. Black circles on the diagram represent positions where GK^{G230D} is soluble and white diamonds represent positions where GK^{G230D} is insoluble. (C) Larger-format GK^{G230D} rhombohedral crystal in a scale-up diffraction device. The crystal was grown with the reagent 0.3 M magnesium chloride, 0.1 M Tris-HCl (pH 8.5), and 20% PEG 1500. The scale bar represents 100 μm . (D) Elastomeric disk containing crystals mounted on a customized crystal cap for in situ diffraction analysis. This figure was adapted from ref 30. (E) In situ diffraction image of a crystal in a scale-up diffraction device. GK^{G230D} crystallized in space group $P2_1$ with a unit cell of $a = 91.1$ Å, $b = 114.3$ Å, $c = 212.6$ Å, $\beta = 91.1^\circ$ and a mosaicity of 0.27° . The faint powder ring around 7 Å is from X-ray scattering off of the elastomeric material of the diffraction device.

extracted from the rest of the device. The extracted section of the device formed a thin disk that was mounted onto a customized crystal cap, placed directly onto the goniometer head, and data was collected from the crystal through the device (Figure 1D). The crystal in Figure 1C was used for in situ data collection through the scale-up diffraction device and diffracted to 2.0 Å resolution (Figure 1E). The structure of GK^{G230D} was solved using molecular replacement and the statistics for the refined model are reported in Table 1. The entire process from the solubility characterization to the production of diffraction-quality crystals required only 31 μL of sample, corresponding to less than 1 mg of GK^{G230D}.

Structural Overview. GK^{G230D} crystallized in space group $P2_1$ with two tetramers of 222 point symmetry in the asu. The monomers of tetramers I and II are designated O_I, X_I,

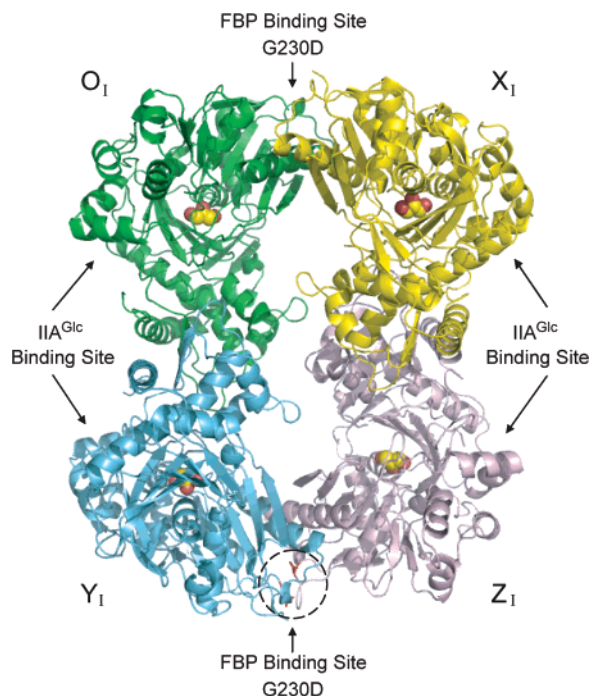


FIGURE 2: Overall structure of GK^{G230D}. GK^{G230D} tetramer I is shown with the O_I, X_I, Y_I, and Z_I monomers colored green, yellow, blue, and pink, respectively. The X_I and Y_I monomers are in the closed conformation, the O_I monomer is in the open conformation, and the Z_I monomer is in the “very open” conformation. The FBP binding sites are located at the top and the bottom of the tetramer in the O_I–X_I and Y_I–Z_I interface loops. The mutation GK^{G230D} is circled and shown in orange using stick representation at the Y_I–Z_I tetramer interface. The IIA^{Glc} binding sites are located at a 3₁₀ helix on each monomer near the dimer interface. Glycerol is shown in a space-filling representation and indicates the location of the active site and the base of the hinge region in each monomer. All structural images were prepared with PyMOL (39).

Y_I, Z_I and O_{II}, X_{II}, Y_{II}, Z_{II}, respectively, following the previously established GK notation (Figure 2). The tertiary structure of tetramers I and II mimics the tetramer geometry seen in an earlier structure of GK that is postulated to be the physiologically relevant tetrameric form of the protein (19). The O–Y and X–Z monomer interfaces are identical to the functional dimer interface seen in GK^{WT} and indicate the O–Y and X–Z monomers also form the functional dimer in GK^{G230D}. Each dimer has one monomer in the closed conformation and one monomer in the open conformation, similar to the putative active conformation of GK seen in the presence of glycerol and ATP analogues (11). The FBP binding loops, located at the O–X and Y–Z tetramer interfaces, are ordered at the Y_I–Z_I tetramer interface in GK^{G230D} and differ significantly from the GK^{WT} FBP binding loops. Monomer domain organization is identical to GK^{WT} and has previously been described (18). All monomers in the asu have a glycerol molecule bound at the cleft of the active site.

The FBP Binding Loops. The G230D mutation in the FBP binding loops (residues 229–236) is ordered at the Y_I–Z_I tetramer interface in the GK^{G230D} structure. The average B factor for the Y_I–Z_I FBP binding loops is 21.1 Å², comparable to the average B factor of 21.2 Å² for the overall structure. Large conformational changes are evident between the GK^{G230D} and GK^{WT} FBP binding loops; the Y–Z loops of GK^{WT} superposition onto the Y_I–Z_I loops of GK^{G230D}

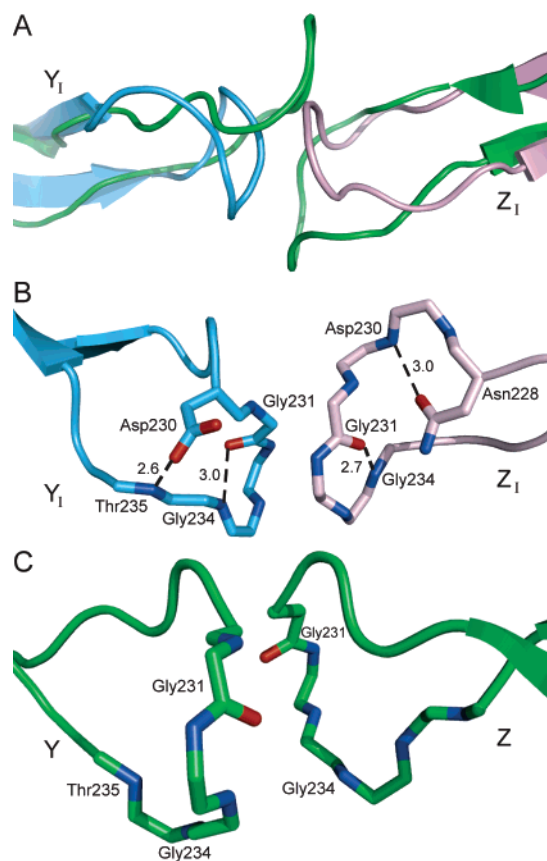


FIGURE 3: Altered FBP binding loop conformations in GK^{G230D}. (A) Comparison of the GK^{G230D} FBP binding loop conformations in GK^{G230D} and GK^{WT}. Residues 225–240 of the Y–Z FBP binding site in GK^{WT} (PDB access code: 1GLF) are superpositioned onto the Y_I–Z_I FBP binding site in GK^{G230D}. The Y_I and Z_I monomers of GK^{G230D} are blue and pink, respectively, and the Y and Z monomers of GK^{WT} are green. (B) Intramolecular hydrogen-bonding networks in the GK^{G230D} FBP binding loops. The Y_I monomer has two hydrogen-bond interactions between Asp230 and Thr235, and between Gly231 and Gly234. The Z_I monomer has two hydrogen-bond interactions between Asn228 and Asp230, and between Gly231 and Gly234. (C) FBP binding loop conformation in GK^{WT} at the Y–Z tetramer interface. Note that GK^{WT} is shown as it appears when aligned to the GK^{G230D} FBP binding loops as displayed in (B).

(residues 225–240) with a C_α root-mean-square deviation (rmsd) of 2.6 Å (Figure 3A). In GK^{WT}, the main chain loop conformations and the side chain positions are identical in monomers Y and Z, creating a symmetrical FBP binding site at the tetramer interface. In GK^{G230D}, the Y_I and Z_I FBP binding loops have unique main chain conformations in each monomer and disrupt FBP binding by eliminating the symmetrical binding pocket for FBP at the tetramer interface.

The wild-type FBP binding loop conformation in GK^{WT} is stabilized through intramolecular and intermolecular loop interactions. The intramolecular loop interactions include hydrogen-bond interactions between O_{δ1} of Asn228 and the backbone amide of Gly230, and between the backbone oxygen of Thr235 and N_ε of Arg236 (19). Intermolecular loop hydrogen-bond interactions also occur across the tetramer interface between N_{δ2} of Asn228 and the backbone oxygen of Gly231, and between the backbone amide of Gly231 and the backbone oxygen of Asn228 in both monomers (19).

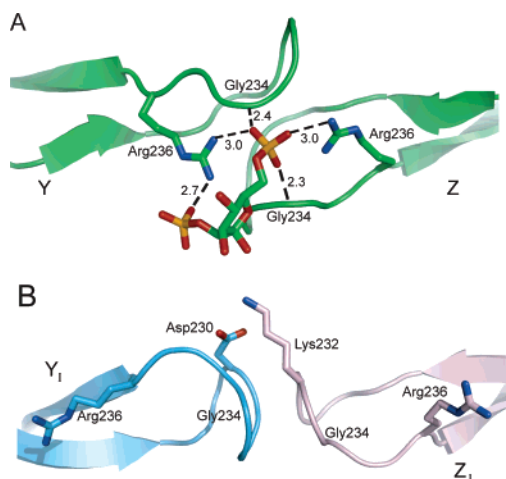


FIGURE 4: Altered FBP binding site in GK^{G230D}. (A) FBP binding mechanism in GK^{WT} at the Y-Z tetramer interface (PDB access code: 1BO5). FBP is positioned between the Y and Z monomers by a network of interactions involving Gly234 and Arg236. FBP is shown in stick representation with the 1-phosphate at the bottom and the 6-phosphate at the top of the image. (B) The Y₁-Z₁ tetramer interface of GK^{G230D}. The Y₁ and Z₁ monomers of GK^{G230D} are blue and pink, respectively. The residues Asp230 of the Y₁ monomer and Lys232 of the Z₁ monomer are positioned at the tetramer interface in GK^{G230D} and disrupt the wild-type FBP binding site. Note that the Arg236 side chains are shifted away from the FBP binding site in both monomers.

Intramolecular hydrogen-bonding networks in the GK^{G230D} FBP binding loops replace the wild-type loop interactions and hold the Y₁ and Z₁ loops in two main chain conformations that are significantly different than in GK^{WT} (Figure 3B). In the Y₁ monomer, there are two hydrogen-bond interactions between O_{δ2} of Asp230 and the backbone amide of Thr235, and between the backbone oxygen of Gly231 and the backbone amide of Gly234. In the Z₁ monomer, there are two hydrogen-bond interactions between O_{δ1} of Asn228 and the backbone amide of Asp230, and between the backbone oxygen of Gly231 and the backbone amide of Gly234. A simplified view of the GK^{WT} FBP binding loops is presented for comparison with the GK^{G230D} intramolecular loop interactions (Figure 3C). Notably, the backbone oxygen atoms of Gly231 in GK^{WT} are involved in intermolecular loop interactions, whereas the backbone oxygen atoms of Gly231 in GK^{G230D} are utilized in intramolecular loop interactions.

The FBP Binding Site. In GK^{WT}, residues Gly234 and Arg236 from each monomer are located at the tetramer interface and are required for FBP binding. Five interactions between GK^{WT} residues Gly234 and Arg236 and the phosphate moieties of FBP occur in the wild-type regulatory binding site (20). The majority of the interactions position the 6-phosphate of FBP at a central location between the two FBP binding loops (Figure 4A). Specifically, N_{η1} of Arg236 in monomer Y interacts with the 6-phosphate of FBP in monomer Y, and N_{η2} of Arg236 in monomer Z interacts with the 6-phosphate of FBP. The 6-phosphate of FBP is also bound by interactions with the backbone amide of Gly234 in monomers Y and Z. Furthermore, N_{η2} of Arg236 in monomer Y interacts with the 1-phosphate of FBP and serves to bridge both phosphate groups of FBP.

The appearance of Asp230 in the FBP binding site of GK^{G230D} repositions the surrounding residues and eliminates

the wild-type FBP binding site (Figure 4B). The C_α of Asp230 is shifted from the wild-type C_α of Gly230 by 4.3 Å in the Y₁ monomer of GK^{G230D}. In addition, the C_α of Lys232 in the Z₁ monomer is shifted by 10.3 Å from the wild-type position and appears at the tetramer interface in GK^{G230D}. To accommodate Asp230 and Lys232 in the FBP binding site, the FBP binding residues Gly234 and Arg236 are shifted away from their wild-type FBP binding positions in each of the monomers. The C_α of Gly234 is shifted by 3.3 Å in the Z₁ monomer and the N_ε of Arg236 is shifted by 9.7 Å in the Y₁ monomer of GK^{G230D}. The repositioning of the FBP binding residues Gly234 and Arg236 to the outside of the FBP binding site could explain why a decrease in FBP inhibition is observed for GK^{G230D}.

The Oligomeric State of GK^{G230D}. To further explore the decreased FBP inhibition and increased activity of GK^{G230D}, light scattering was used to compare the oligomeric states of GK^{G230D} and GK^{WT} in the presence and in the absence of FBP. In the absence of FBP, the GK^{G230D} sample contained a principal dimer peak with a molecular weight of 113 ± 1 kDa and a secondary tetramer peak of 227 ± 16 kDa that was ~2% (estimated mass) of the principal peak (Figure 5A). Under the same conditions, the GK^{WT} sample had a principal dimer peak with a molecular weight of 177 ± 1 kDa and a secondary peak of 391 ± 4 kDa that comprised ~9% (estimated mass) of the total sample. The GK^{WT} dimer peak eluted ~0.3 mL later than the GK^{G230D} dimer peak and the GK^{WT} secondary peak was more predominant than in GK^{G230D}. The secondary peak of GK^{WT} likely represents a tetramer species mixed in with some higher molecular weight species, as indicated by the sharp rise in the molecular weight versus volume plot. The later elution time for the GK^{WT} dimer peak is indicative of a dynamic dimer-tetramer species, in contrast to the predominantly dimeric species in the GK^{G230D} sample.

In the presence of FBP, the GK^{G230D} sample had a principal dimer peak with a molecular weight of 127 ± 3 kDa and an aggregate peak with ~1/4 the mass that contained species ranging from 200 to 800 kDa (Figure 5B). The GK^{WT} sample eluted as two peaks in the presence of FBP: one large aggregate peak just after the dead volume and a second peak that did not completely resolve from the aggregation peak. The aggregate peak contained species in excess of 1 Mda. The second peak had a molecular weight of 328 ± 10 kDa and is similar to the tetramer + aggregate peak observed in the absence of FBP. The addition of FBP to the elution buffer appeared to create a certain degree of nonhomogenous aggregation for both of the samples. Despite the aggregation, the GK^{G230D} sample was primarily dimeric, whereas the GK^{WT} dimeric species was completely eliminated in the presence of FBP.

The IIA^{Glc} Binding Site. The IIA^{Glc} binding site adopts the IIA^{Glc}-free conformation seen in GK^{WT} in all of the GK^{G230D} monomers with the exception of the O₁ monomer. In the absence of IIA^{Glc}, residues 473–475 have a random coil conformation and residues 476–501 form the C-terminal α-helix. In the presence of IIA^{Glc}, residues 473–478 are shifted into a 3₁₀ helix and the C-terminal α-helix begins at residue 479 (19). A crystal contact at Arg402 in the O₁ monomer, supplied by an X₁ symmetry operator, alters the conformation of O₁ at the IIA^{Glc} binding site to form the 3₁₀ helix seen when IIA^{Glc} is present. The crystal contact at

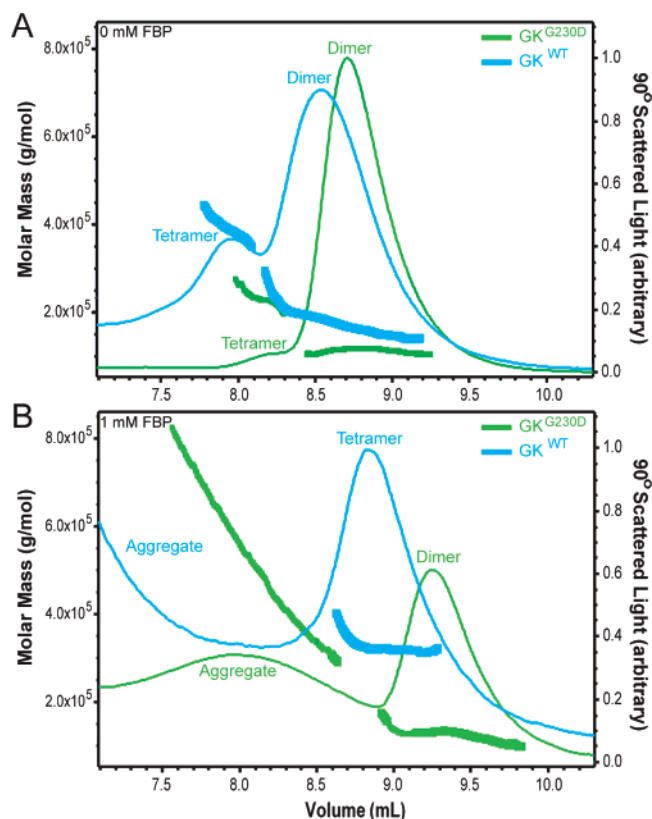


FIGURE 5: Size exclusion chromatography - multi-angle laser light scattering studies (SEC-MALLS) of GK^{G230D} and GK^{WT} . (A) Light scattering results for GK^{G230D} and GK^{WT} in the absence of FBP. GK^{G230D} is shown in green and exists primarily as dimers with a very slight amount of tetramers in a $\sim 140:1$ molar ratio. GK^{WT} is shown in blue and exists as a mixture of dimers and tetramers in a $\sim 10:1$ molar ratio. The molecular weight of each species was determined on a gel filtration column using a light scattering setup as described in Experimental Procedures. The thin continuous line represents the signal from the right angle scattered light and is similar to the UV trace usually presented for protein chromatography. It should be noted that the scattered light is proportional to the square of the molecular weight, so heavier species are disproportionately represented on the plot. The heavier discontinuous lines plot the molecular weight determinations of the protein eluting from the column at that particular time. (B) Light scattering results for GK^{G230D} and GK^{WT} in the presence of 1 mM FBP. GK^{G230D} remained a primarily dimeric species, while GK^{WT} was primarily tetrameric and contained no dimeric species. The addition of FBP to the elution buffer also caused a certain degree of nonhomogenous aggregation for both GK^{G230D} and GK^{WT} , forming species with molecular weights ranging from ~ 400 to greater than 1000 kDa. Note that the GK^{G230D} dimer peak was eluted ~ 0.7 mL later and the GK^{WT} tetramer peak was eluted ~ 1 mL later than the corresponding peaks observed in the absence of FBP.

Arg402 appears to be inducing the structural rearrangements that occur upon IIA^{Glc} binding.

Changes in Quaternary Structure. The quaternary structure of GK^{G230D} is similar to that seen in GK^{WT} . The functional dimer interfaces of O_I-Y_I , X_I-Z_I , $O_{II}-Y_{II}$, and $X_{II}-Z_{II}$ are identical to the $O-Y$ and $X-Z$ interfaces of GK^{WT} . GK^{G230D} tetramers I and II have an almost identical quaternary structure, verified by the low 2.0 Å C_α rmsd between the tetramers. The GK^{WT} tetramer superpositions onto GK^{G230D} tetramers I and II with a C_α rmsd of 3.6 and 3.3 Å, respectively. The primary deviations in the quaternary structure of GK^{G230D} and GK^{WT} arise from changes at the tetramer interface as a result of the G230D mutation at the

FBP binding site. It should be noted that while GK^{G230D} crystallized as a tetramer, the light scattering analysis demonstrated that GK^{G230D} exists primarily as a dimer (Figure 4). The GK^{G230D} structure is not the first example of a GK mutant crystallizing as a tetramer when it was shown to exist as a dimer in solution (11, 19).

Domain Motion. The eight monomers in the glycerol bound GK^{G230D} structure ($GK^{G230D}\cdot gly$) exhibit a range of open and closed conformations. The X_I and Y_I monomers in $GK^{G230D}\cdot gly$ have a main chain conformation identical to the closed conformation of GK^{WT} and the O_I and O_{II} monomers have a main chain conformation identical to the open conformation previously seen in the structure of a GK mutant with both glycerol and the nonhydrolyzable ATP analogue phosphodifluoromethylphosphonic acid-adenylate ester bound ($GK^{S58W}\cdot gly\cdot ATF$) (11). The X_{II} and Y_{II} monomers exist in an intermediate conformation between the closed and open conformation, and the Z_I and Z_{II} monomers adopt a more open, or “very open”, conformation than is seen in the previously reported open conformation.

Domain motion analysis of the $GK^{S58W}\cdot gly\cdot ATF$ structure revealed a difference of $\sim 6^\circ$ between the open and closed form of the GK monomers. The $GK^{G230D}\cdot gly$ structure exhibited a larger difference between the open and closed forms, with rotations between monomer domains I and II in the range of 10 to 18° . The larger difference observed for the $GK^{G230D}\cdot gly$ open versus closed state is more in line with the $\sim 12^\circ$ rotation observed for the yeast hexokinase structure (13). The motion in the yeast hexokinase structure was, however, attributable to the binding of glucose. The motion in the $GK^{G230D}\cdot gly$ structure cannot be attributed to the binding of glycerol since the large domain motion occurred with glycerol bound to all of the individual protomers. Thus, it appears that unlike hexokinase, the binding of glycerol alone to glycerol kinase does not influence the open versus closed state of the molecule.

In contrast to the wide range of conformations observed for the binary complex $GK^{G230D}\cdot gly$, the structure representing the ternary complex $GK^{S58W}\cdot gly\cdot ATF$ was observed to exist within a rather narrow range of domain orientations. Apparently, glycerol kinase does not adopt a catalytically competent conformation until both glycerol and nucleotide are bound within the active site. A comparison between the closed form, as represented by the Y protomer from $GK^{S58W}\cdot gly\cdot ATF$, and the open form as represented by the either the O_{II} or Z_{II} protomers from $GK^{G230D}\cdot gly$, indicates that there is a $\sim 14^\circ$ rigid body rotation that occurs upon nucleotide binding (Table 2). This is comparable to the value observed between the open and closed state of yeast hexokinase structure, suggesting that nucleotide triphosphate binding is the determining factor in creating the “closed” state of the molecule.

DISCUSSION

Use of the microfluidic crystallization platform allowed us to determine the high-resolution structure of GK^{G230D} using less than 1 mg of protein, significantly less than is required using traditional crystallization techniques. The solubility screening and phase diagram measurements consumed ~ 200 μ g of protein, the crystal screening and optimization consumed ~ 250 μ g, and the crystal scale-up consumed ~ 450

Table 2: Domain Rotation for GK^{G230D}

pair	rotation angle	rmsd (Å)
Y _I –O _I	15.5	1.6
X _I –Z _I	18	1.8
Y _{II} –O _{II}	11.3	1.0
X _{II} –Z _{II}	10.0	1.5
BWF ^b – Y _I ^c	n.d.	0.5
BWF – X _{II} ^d	7.2	0.9
BWF – O _{II}	14.7	1.5
BWF – Z _{II}	14.3	1.5

^a Used Hingefind algorithm to determine effective motion of domains. Used a partition value of 1.8 Å with the VMD implementation. Automatically determined domains were essentially identical to previous analysis (11). ^b BWF monomer Y was used for all calculations. ^c BWF – Y_I: no difference (n.d.) between BWF and Y_I protomer. ^d Rotation axis for X_{II} is not the same as the rotation axis for O_{II} and Z_{II}.

μg. Vapor diffusion crystallization experiments with the same crystallization reagent were performed in parallel to compare the diffraction limits of crystals grown in the scale-up diffraction devices to crystals grown in traditional formats. The vapor diffusion crystallization experiments produced rhombohedral crystals of dimensions 1000 μm × 500 μm × 500 μm that diffracted to 3.0 Å resolution (with unit cell $a = 91.3$ Å, $b = 102.9$ Å, $c = 222.6$ Å, $\beta = 90.6^\circ$ and a mosaicity of 0.64°) in the same space group as the diffraction device crystals. The vapor diffusion crystals were not used for structure determination due to the higher quality of the crystals grown in the scale-up diffraction devices. The higher diffraction resolution (2.0 Å) and lower mosaicity (0.27°) of the crystals grown in the microfluidic devices probably results from two factors: the crystal growth kinetics of the free interface diffusion crystallization experiments and the avoidance of crystal damage, a corollary of crystal harvesting, in situ data collection from the diffraction devices.

GK^{G230D} provides the first structural overview of a GK variant with a mutation in the FBP binding site and is the first glycerol kinase structure where the FBP binding loops are ordered in the absence of a bound FBP or buffer molecule. GK^{G230D} contains an altered interaction network at the tetramer interface that replaces the wild-type FBP binding site. Most notably, the FBP binding loops in GK^{G230D} adopt a conformation different from what is observed in the wild-type enzyme. The GK^{G230D} FBP binding loop conformations are supported through a series of intramolecular hydrogen-bond interactions in each of the FBP binding loops. Additionally, residues Asp230 and Lys232 are found at the tetramer interface in GK^{G230D}, whereas the wild-type FBP binding residues Gly234 and Arg236 are directed away from the FBP binding site. The structural changes at the FBP binding site eliminate the wild-type FBP binding pocket at the tetramer interface and as a result decrease FBP inhibition in GK^{G230D}.

The existence of an active dimer form and an inactive tetramer form of GK^{WT} shows an inherent link between the oligomeric state of the protein and its activity. Since the crystal structure did not elucidate a reasonable explanation for the enhanced enzymatic activity observed for GK^{G230D}, we used light scattering studies to probe the oligomeric state of the protein. We found that in the absence of FBP, GK^{G230D} exists primarily as a dimer with only a trace amount of tetramer species while GK^{WT} exists as a dynamic mixture of dimers and tetramers. The dimers observed for GK^{WT}

disappeared upon the addition of FBP, whereas the GK^{G230D} dimer population was essentially unaffected. Since GK^{WT} FBP inhibition is dependent upon tetramer formation, the absence of a GK^{G230D} tetramer species in the presence of FBP is consistent with the decreased FBP inhibition of GK^{G230D}. Furthermore, the higher proportion of GK^{G230D} dimer species in the absence of FBP and the resistance of GK^{G230D} dimers to tetramer formation in the presence of FBP suggest the primarily dimeric state of the enzyme is responsible for the increased activity of GK^{G230D}. Given the light scattering results, the GK^{G230D} tetramer in the crystal structure is probably the result of crystal packing energetics and most likely reflects one of potentially multiple dimer–dimer interactions that occur.

It should be noted that the functional implications of the mutation cannot be completely established based on the ordered Y_I–Z_I FBP binding site given the appearance of disordered binding sites in the structure. The light scattering results confirmed GK^{G230D} is primarily dimeric in solution and suggest GK^{G230D} dimers form fleeting dimer–dimer interactions in solution that are unlikely to persist on a long time scale. Given the transient nature of the dimer–dimer interactions in solution, the ordered tetramer interface most likely depicts only one of many dimer–dimer interactions that occur at the FBP binding site of GK^{G230D} in solution. The general structural rearrangements in the GK^{G230D} Y_I–Z_I FBP binding loops reveals two ways in which the FBP binding site is altered: novel main chain loop conformations that disrupt the wild-type FBP binding pocket, and the repositioning of residues responsible for FBP binding away from the FBP binding site. Both types of structural rearrangements seen in the Y_I–Z_I FBP binding loops provide a plausible explanation for the altered FBP regulation in GK^{G230D}, and other loop interactions based on one or both of these structural alterations could account for other fleeting dimer–dimer interactions that occur between GK^{G230D} dimers in solution.

GK^{G230D} also provides the first structural evidence of multiple GK monomer conformations in the presence of glycerol and in the absence of a nucleotide substrate. Previous monomer domain motion analysis of a GK^{S58W}·glyc·ATF variant identified an open and closed conformation for GK monomers in the presence of glycerol and ATF. The open and closed monomer conformations were observed in the GK^{G230D}·glyc structure, and in addition a new “very open” conformation of the enzyme hypothesized to exist in the absence of a bound nucleotide was evident in monomers Z_I and Z_{II}. The multiple GK^{G230D}·glyc monomer conformations conclusively demonstrate glycerol binding does not restrict the domain motion of GK monomers and confirms nucleotide binding is the determining factor in locking GK into the closed form required for enzyme activity.

In conclusion, the crystal structure of GK^{G230D} is the first demonstration of in situ structure determination for a novel crystallization target using a microfluidic crystallization platform. The GK^{G230D} structure revealed an altered interaction network at the tetramer interface that is responsible for disrupting the FBP binding site and decreasing the allosteric regulation of GK^{G230D} by FBP. The oligomeric state of GK^{G230D} was investigated with light scattering and showed the increased enzymatic activity is a result of the stable dimeric quaternary state of GK^{G230D}. Last, domain motion

analysis revealed a wide range of GK^{G230D} monomer conformations in the presence of glycerol and verified glycerol binding is not responsible for inducing the conformational change and locking GK into a catalytically active conformation.

ACKNOWLEDGMENT

Portions of this research were carried out at the Stanford Synchrotron Radiation Laboratory, a national user facility operated by Stanford University on behalf of the U.S. Department of Energy, Office of Basic Energy Sciences. The SSRL Structural Molecular Biology Program is supported by the Department of Energy, Office of Biological and Environmental Research, and by the National Institutes of Health, National Center for Research Resources, Biomedical Technology Program, and the National Institute of General Medical Sciences.

REFERENCES

- Ibarra, R. U., Edwards, J. S., and Palsson, B. O. (2002) *Escherichia coli* K-12 undergoes adaptive evolution to achieve *in silico* predicted optimal growth, *Nature* **420**, 186–189.
- Honisch, C., Raghunathan, A., Cantor, C. R., Palsson, B. O., and van den Boom, D. (2004) High-throughput mutation detection underlying adaptive evolution of *Escherichia coli*-K12, *Genome Res.* **14**, 2495–2502.
- Herring, C. D., Raghunathan, A., Honisch, C., Patel, T., Applebee, M. K., Joyce, A. R., Albert, T. J., Blattner, F. R., van den Boom, D., Cantor, C. R., and Palsson, B. O. (2006) Comparative genome sequencing of *Escherichia coli* allows observation of bacterial evolution on a laboratory timescale, *Nat. Genet.* **12**, 1406–1412.
- Zwaig, N., Kistler, W. S., and Lin, E. C. C. (1970) Glycerol kinase, the pacemaker for the dissimilation of glycerol in *Escherichia coli*, *J. Bacteriol.* **102**, 753–759.
- Lin, E. C. C., Koch, J. P., Chused, T. M., and Jorgensen, S. E. (1962) Utilization of L- α -glycerophosphate by *Escherichia coli* without hydrolysis, *Proc. Nat. Acad. Sci. U.S.A.* **48**, 2145–2150.
- de Riel, J. K., and Paulus, H. (1978a) Subunit dissociation in the allosteric regulation of glycerol kinase from *Escherichia coli*. 1. Kinetic evidence, *Biochemistry* **17**, 5134–5140.
- de Riel, J. K., and Paulus, H. (1978b) Subunit dissociation in the allosteric regulation of glycerol kinase from *Escherichia coli*. 2. Physical evidence, *Biochemistry* **17**, 5141–5145.
- de Riel, J. K., and Paulus, H. (1978c) Subunit dissociation in the allosteric regulation of glycerol kinase from *Escherichia coli*. 3. Role in desensitization, *Biochemistry* **17**, 5146–5150.
- Pettigrew, D. W., Yu, G.-J., and Liu, Y. (1990) Nucleotide regulation of *Escherichia coli* glycerol kinase: initial-velocity and substrate binding studies, *Biochemistry* **29**, 8620–8627.
- Hurley, J. H. (1996) The sugar kinase/heat shock protein 70/actin superfamily: implications of conserved structure for mechanism, *Annu. Rev. Biophys. Biomol. Struct.* **25**, 137–162.
- Bystrom, C. E., Pettigrew, D. W., Branchaud, B. P., O'Brien, P., and Remington, S. J. (1999) Crystal structure of *Escherichia coli* glycerol kinase variant S58 \rightarrow W in complex with nonhydrolyzable ATP analogues reveal a putative active conformation of the enzyme as a result of domain motion, *Biochemistry* **38**, 3508–3518.
- Thorner, J. W., and Paulus, H. (1973) Catalytic and allosteric properties of glycerol kinase from *Escherichia coli*, *J. Biol. Chem.* **248**, 3922–3932.
- Bennett Jr., W. S., and Steitz, T. A. (1978) Glucose-induced conformational change in yeast hexokinase, *Proc. Natl. Acad. Sci. U.S.A.* **75**, 4848–4852.
- Chik, J. K., Lindberg, U., and Schutt, C. E. (1996) The structure of an open state of b-actin at 265 Å resolution, *J. Mol. Biol.* **263**, 607–623.
- Postma, P. W., Epstein, W., Schuitema, A. R. J., and Nelson, S. O. (1984) Interaction between III^{Glc} of the phosphoenolpyruvate: sugar phosphotransferase system and glycerol kinase of *Salmonella typhimurium*, *J. Bacteriol.* **158**, 351–353.
- Novotny, M. J., Frederickson, W. L., Waygood, E. B., and Saier, M. H., Jr. (1985) Allosteric regulation of glycerol kinase by enzyme III^{Glc} of the phosphotransferase system in *Escherichia coli* and *Salmonella typhimurium*, *J. Bacteriol.* **162**, 810–816.
- Zwaig, N., and Lin, E. C. C. (1966) Feedback inhibition of glycerol kinase, a catabolic enzyme in *Escherichia coli*, *Science* **153**, 755–757.
- Hurley, J., Faber, H., Worthylake, D., Meadow, N., Roseman, S., Pettigrew, D., and Remington, S. (1993) Structure of the regulatory complex of *Escherichia coli* III^{Glc} with glycerol kinase, *Science* **259**, 673–677.
- Feese, M. D., Faber, H. R., Bystrom, C. E., Pettigrew, D. W., and Remington, S. J. (1998) Glycerol kinase from *Escherichia coli* and an Ala65 \rightarrow Thr mutant: the crystal structures reveal conformational changes with implications for allosteric regulation, *Structure* **6**, 1407–1418.
- Ormo, M. O., Bystrom, C. E., and Remington, S. J. (1998) Crystal structure of a complex of *Escherichia coli* glycerol kinase and an allosteric effector fructose 1,6-bisphosphate, *Biochemistry* **37**, 16565–16572.
- Pettigrew, D. W., Ma, D. P., Conrad, C. A., and Johnson, J. R. (1988) *Escherichia coli* glycerol kinase. Cloning and sequencing of the glpK gene and the primary structure of the enzyme, *J. Biol. Chem.* **263**, 135–139.
- Pettigrew, D., Liu, W., Holmes, C., Meadow, N., and Roseman, S. (1996) A single amino acid change in *Escherichia coli* glycerol kinase abolishes glucose control of glycerol utilization *in vivo*, *J. Bacteriol.* **178**, 2846–2852.
- Liu, W., Faber, H. R., Feese, M. D., Remington, S. J., and Pettigrew, D. W. (1994) *Escherichia coli* glycerol kinase: role of a tetramer interface in regulation by fructose 1,6-bisphosphate and phosphotransferase system regulatory protein III^{Glc}, *Biochemistry* **33**, 10120–10126.
- Faber, H. R., Pettigrew, D. W., and Remington, S. J. (1989) Crystallization and preliminary X-ray studies of *Escherichia coli* glycerol kinase, *J. Mol. Biol.* **207**, 637–639.
- Hames, C., Halbedel, S., Schilling, O., and Stulke, J. (2005) Multiple-mutation reaction: a method for simultaneous introduction of multiple mutations into the glpK gene of *Mycoplasma pneumoniae*, *Appl. Environ. Microbiol.* **71**, 4097–4100.
- Wyatt, P. J. (1993) Light scattering and the absolute characterization of macromolecules, *Anal. Chim. Acta* **272**, 1–40.
- Zhu, H., Ownby, D. W., Riggs, C. K., Nolasco, N. J., Stoops, J. K., and Riggs, A. F. (1996) Assembly of the gigantic hemoglobin of the earthworm *Lumbricus terrestris*, *J. Biol. Chem.* **271**, 30007–30021.
- Hansen, C. L., Sommer, M. O. A., and Quake, S. R. (2004) Systematic investigation of protein phase behavior with a microfluidic formulator, *Proc. Natl. Acad. Sci. U.S.A.* **101**, 14431–14436.
- Anderson, M. J., Hansen, C. L., and Quake, S. R. (2006) Phase knowledge enables rational screens for protein crystallization, *Proc. Nat. Acad. Sci. U.S.A.* **103**, 16746–16751.
- Hansen, C. L., Classen, S., Berger, J. M., and Quake, S. R. (2006) A microfluidic device for kinetic optimization of protein crystallization and *in situ* structure determination, *J. Am. Chem. Soc.* **128**, 3142–3143.
- Otwinowski, Z., and Minor, W. (1997) Processing X-ray diffraction data collection in oscillation mode, *Methods Enzymol.* **276**, 307–326.
- Brunker, A. T., Adams, P. D., Clore, G. M., DeLano, W. L., Gros, P., Grosse-Kunstleve, R. W., Jiang, J.-S., Kuszewski, J., Nilges, M., Pannu, N. S., Read, R. J., Rice, L. M., Simonson, T., and Warren, G. L. (1993) Crystallography & NMR system: a new software suite for macromolecular structure determination, *Acta Crystallogr. D* **49**, 905–921.
- Jones, T. A., Zou, J.-Y., Cowan, S. W., and Kjeldgaard, M. (1991) Improved methods for building protein models in electron density maps and the location of errors in these models, *Acta Crystallogr. A* **47**, 110–119.
- Lovell, S. C., Davis, I. W., Arendall, W. B., III, de Bakker, P. I., Word, J. M., Prisant, M. G., Richardson, J. S., and Richardson, D. C. (2003) Structure validation by Alpha geometry: phi, psi and Cbeta deviation, *Proteins* **50**, 437–450.
- Winn, M. D., Isupov, M. N., and Murshudov, G. N. (2001) Use of TLS parameters to model anisotropic displacements in macromolecular refinement, *Acta Crystallogr. D* **57**, 122–133.
- Wriggers, W., and Schulten, K. (1997) Protein domain movements: detection of rigid domains and visualization of hinges in

- comparisons of atomic coordinates, *Proteins: Struct., Funct., Genet.* 29, 1–14.
37. Hansen, C. L., Skordalakes, E., Berger, J. M., and Quake, S. R. (2002) A robust and scalable microfluidic metering method that allows protein crystal growth by free interface diffusion, *Proc. Natl. Acad. Sci. U.S.A.* 99, 16531–16536.
38. Brunger, A. (1993) Assessment of phase accuracy by cross validation: the free R value, *Acta Crystallogr. D* 49, 24–36.
39. DeLano, W. L. (2002) DeLano Scientific, San Carlos, CA.

BI700096P